DESIGN, REALIZATION AND LOW POWER RF TESTS OF THE C BAND STRUCTURE PROTOTYPE FOR SPARC

D. Alesini, M. Ferrario, V. Lollo, R. Di Raddo (LNF, INFN)
V. Spizzo and L. Palumbo (Univ. of Rome "La Sapienza")

Abstract

The energy upgrade of the SPARC photo-injector from 170 to 240 MeV will be done by replacing a low gradient S-Band structure with two C-band sections. The structures are traveling wave constant impedance sections, have symmetric axial input couplers and have been optimized to work with a SLED RF input pulse. The paper presents the design criteria of the structures, the single cell parameter optimization and the coupler design. We also illustrate the realization procedure and the low power RF test results on the prototype we have realized for high gradient test performed at KEK (Japan).

1   INTRODUCTION

The SPARC energy will be upgraded from ~170 to more than 240 MeV by replacing a low gradient S-band travelling wave section with two C-band structures. The implementation of this system at SPARC has been proposed to explore the C Band acceleration combined with an S Band injector that, at least from beam dynamics simulations [12] seems to be very promising for the achievable beam quality. The C Band acceleration allows, in principle, obtaining higher gradients and a shorter LINAC, and also this point can be attractive for future upgrades of the SPARC photo-injector. Other important laboratories have proposed the use of the C Band technology for future FELs, like PSI [13], or have already adopted a C Band LINAC for FEL, like Spring 8, Japan [14]. Synergies with these laboratories have been also considered and collaborations have been started on this topic [15].

The new SPARC schematic layout, after the implementation of the C-band system [16], is shown in Fig. 1. Two traveling wave (TW) sections, 1.4 m long, will be installed in the LINAC and will be fed by a C-band klystron manufactured by Toshiba Ltd. The main Toshiba Klystron ET37202 specifications are given in Table I. The HV pulsed modulator and the 400 W driver for the klystron have been manufactured by ScandiNova and MitecTelecom. The system will include also a SLED for power amplification.

The main goal of this installation will be the energy upgrade of the SPARC injector with an average accelerating field >35 MV/m. This means a total energy gain in the two sections >100 MeV.

Before the construction of the final structures a prototype with a reduced number of cells has been realized. The goals of this prototype were the test of all design and construction procedure and the test of the structure at high power at KEK (Japan) in the framework of the collaboration between LNF and KEK.

In the first section of the paper we present the design of the single cell. The coupler design is illustrated in the second section while the realization procedure of the prototype and the low power RF measurements are presented in the last section.

FIG. 1: sketch of the SPARC layout after with the C-band system installation.

TABLE I: Toshiba Klystron ET37202 specifications

Frequency	5712 MHz
Output RF power	50 MW (max).
RF pulse length	2.5 μsec
Pulse rep. rate	50 pps max.
Gain	44 dB min
Efficiency	40 % min
Drive power	300 W

2   SINGLE CELL DESIGN

It is quite easy to understand that, if a constant impedance [2] TW section is fed by a SLED pulse [1], it is possible to obtain a quasi-uniform accelerating field along the structure. In this case, indeed, the "trapezoidal" profile of the RF pulse traveling along the structure is partially compensated by the structure attenuation and the final field profile can be almost uniform.
To have the same uniformity with a constant gradient structure a modulation of the phase of the RF pulse is needed to have a constant output power. On the contrary, if a constant gradient structure is fed by a "classical" SLED pulse, there is an unbalance of the accelerating field between the head and the tail of the section exactly equal to the square-root of the input power.
Another advantage of a constant impedance structure is the fact that the cells are all equal and this reduces the fabrication cost.
For these reasons, and also because we operate SPARC in the single bunch mode, we decided to design constant impedance sections for the energy upgrade in C Band.
As a first step we have calculated the single cell parameters as a function of the iris aperture and thickness considering the $2\pi/3$ accelerating mode. Then we have calculated the main field profile properties in term of average accelerating and surface peak field assuming a SLED input power profile. The whole procedure is discussed in detail below and similar calculations can be also found in [10].

2.1   Single cell parameters

The sketch of the single cell with its main dimensions is given in Fig. 2.
The main figures of merit for a single cell are given below:

$$Z = \frac{E_{acc}^2}{P_{in}} \qquad \text{series impedance}$$

$$\alpha = \frac{p_{diss}}{2P_{in}} \qquad \text{field attenuation constant}$$

$$v_g = \frac{P_{in}}{w} \qquad \text{group velocity}$$

$$r = \frac{E_{acc}^2}{p_{diss}} \qquad \text{shunt impedance per unit length}$$

where:

$$eV_z = e\left|\int_0^D E_z \cdot e^{j\varpi\frac{z}{c}}dz\right|$$ is the single cell energy gain

E_z is the complex accelereting field on axis

$$E_{acc} = \frac{V_z}{D} = \frac{\left|\int_0^D E_z \cdot e^{j\varpi\frac{z}{c}}dz\right|}{D}$$ is the accelerating field in the cell

$$P_{in} = \int_S \frac{1}{2}\mathrm{Re}\left(\underline{E}\times\underline{H}^*\right)\cdot\hat{z}dS$$ is the average input power (flux power)

$$P_{diss} = \frac{1}{2}R_s \int_{S_{ext}}\left|H_{\tan}\right|^2 dS_{ext}$$ is the average dissipated power in the cell

$$p_{diss} = \frac{P_{diss}}{D}$$ is the average dissipated power per unit length

$$W = \frac{1}{4}\mu_0\int_V \underline{H}\cdot\underline{H}^* dV + \frac{1}{4}\varepsilon_0\int_V \underline{E}\cdot\underline{E}^* dV$$ is the stored energy in the cell

$$w = \frac{W}{D}$$ is the average stored energy per unit length

The series impedance, field attenuation, group velocity and the ratio between the maximum surface electric field and the accelerating one are reported in Fig. 3 as a function of the irises half aperture (a) and thickness (t). They have been found using the 2D electromagnetic code SUPERFISH [4] and the procedure illustrated in [5] to calculate the traveling wave parameters from standing wave simulations. In particular the use of the 2D code SUPERFISH allowed a better calculation [6] of the surface electric field on the iris with respect to 3D codes like HFSS [7].

Fig. 4 shows the ratio E_{s_max}/E_{acc} as a function of the iris ellipticity for the iris values a=7 mm and t=2.5 mm. Similar results have been obtained for other iris apertures. The plot shows that for a certain iris aperture there is an optimum elliptical profile of the iris itself that minimizes the surface field. The maximum reduction of the surface field is of the order of 8%.
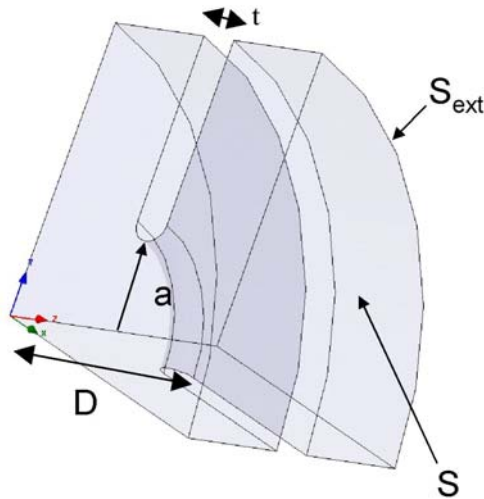
FIG. 2: sketch of the single cell with main parameters.
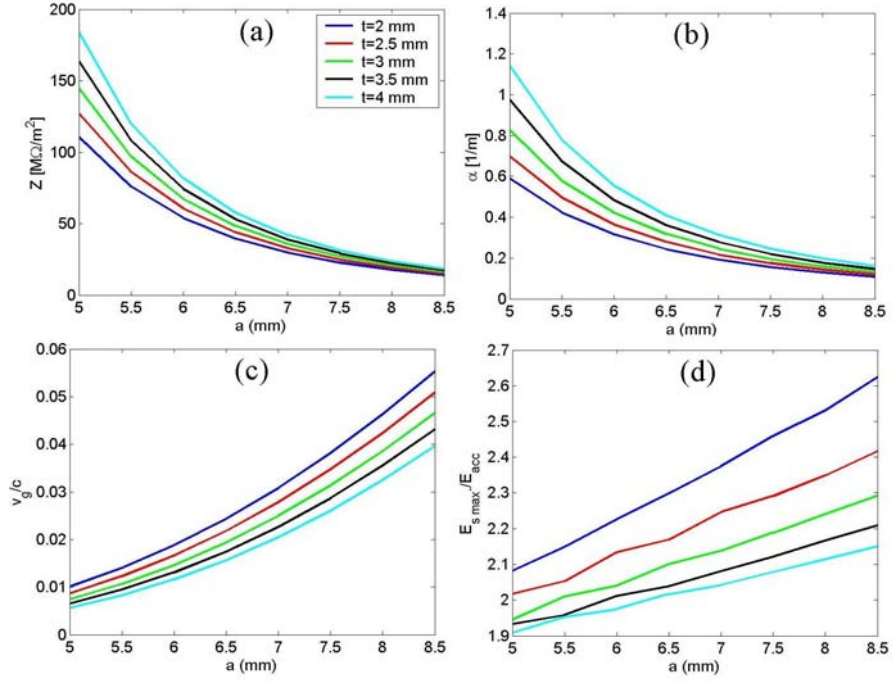
FIG. 3: Single cell parameters as a function of the iris dimension and thickness: (a) series impedance; (b) field attenuation constant; (c) group velocity; (d) maximum surface electric field normalized to the accelerating field.
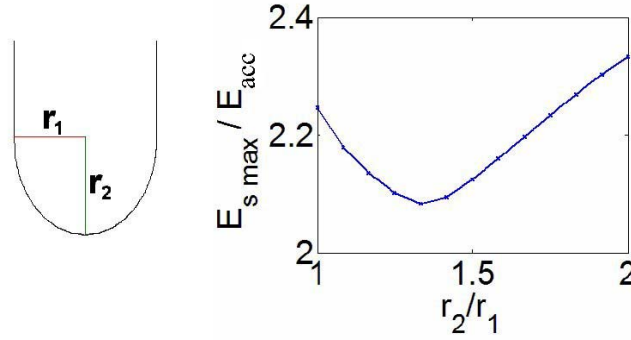

FIG. 4: Maximum surface electric field normalized to the average accelerating field as a function of the iris ellipticity (case: a=7 mm and t=2.5 mm).

2.2 SLED input pulse

The peak power from the SLED is given by the following formula [1]:

$$P_{SLEDout}(t) = P_{KLYout}\left[\underbrace{\frac{2\beta}{1+\beta}\left(2 - e^{-t_1/\tau}\right)e^{-t/\tau}}_{G} - \underbrace{\frac{\beta-1}{\beta+1}}_{A}\right]^2 = P_{KLYout}\left[Ge^{-t/\tau} - A\right]^2$$

(1)

where P_{KLYout} is the output power from the klystron, t_1 is the time of the phase switch, G is the so called SLED gain, $\tau = 2Q_L/\omega_{RF}$ is the decay time, β is the coupling coefficient of the

SLED cavity, $Q_L = Q_0 / (1 + \beta)$ is the loaded quality factor with Q_0 the unloaded quality factor.

In our particular case the SLED feeds two sections and therefore the input power into the TW structure as a function of time is:

$$P_{TW}(t) = \frac{P_{SLEDout}(t)}{2} = \underbrace{\frac{P_{KLYout}}{2}}_{P_{TW\_0}} \left[G e^{-t/\tau} - A \right]^2$$

(2)

The power flux along a constant impedance TW structure as a function of the longitudinal coordinate (z) and time (t) is then:

$$\begin{cases} P_{TW}(z,t) = P_{TW}(t - z/v_g) e^{-2\alpha z} & z \le t v_g \\ P_{TW}(z,t) = 0 & z > 0 \end{cases}$$

(3)

The corresponding accelerating field is give by:

$$\begin{cases} E_{acc}(z,t) = \sqrt{ZP_{TW}(t - z/v_g)} e^{-\alpha z} = \sqrt{ZP_{TW\_0}} \left(G e^{-\frac{t - z/v_g}{\tau}} - A \right) e^{-\alpha z} & z \le t v_g \\ E_{acc}(z,t) = 0 & z > t v_g \end{cases}$$

(4)

The peak surface field occurs at the entrance of the structure and at the beginning of the input pulse. Knowing, for example, the ratio $E_{s\,max}/E_{acc}$ (shown in Fig. 3(d)) the maximum surface field is simply given by:

$$E_{s\_peak} = \left(\frac{E_{s\_max}}{E_{acc}} \right) E_{acc}(0,0) = \left(\frac{E_{s\_max}}{E_{acc}} \right) \sqrt{ZP_{TW\_0}} (G - A)$$

(5)

while the accelerating field distribution after one filling time $\tau_F = L/v_g$ is:

$$E_{acc}(z) = E_{acc}(z, t = L/v_g) = \sqrt{ZP_{TW\_0}} \left(G e^{\frac{z-L}{v_g \tau}} - A \right) e^{-\alpha z}$$

(6)

where L is the structure length.

From eq. (6) it is easy to calculate the total beam energy gain in the structure (eV$_{TOT}$) and the average accelerating field:

$$eV_{TOT} = e \int_0^L E_{acc} dz = e \sqrt{ZP_{TW\_0}} \left(G \frac{e^{-\frac{\tau_F}{\tau}} - e^{-\alpha L}}{\alpha - \frac{1}{v_g \tau}} - A \frac{1 - e^{-\alpha L}}{\alpha} \right)$$

$$E_{acc\_av} = \frac{V_{TOT}}{L}$$

(7)

From eq. (6) it is easy to note that, also in the case of a constant impedance structure, it is not possible to obtain a perfectly uniform accelerating field along the structure because the factor

$\left(Ge^{\frac{z-L}{v_g \tau}} - A \right) e^{-\alpha z}$ cannot be constant with z. Nevertheless the non uniformity of the field between the initial and final parts of the structure is significantly smaller if compared to a constant gradient structure fed by the SLED input pulse. More precisely, the uniformity of the field (FU) can be evaluated with the following ratio:

$$FU = \frac{\left| E_{acc}(0) - E_{acc}(L) \right|}{\left(E_{acc}(0) + E_{acc}(L) \right)/2} \Rightarrow 2 \frac{\left| G\left(e^{-\alpha L} - e^{-\frac{\tau_F}{\tau}} \right) + A\left(1 - e^{-\alpha L}\right) \right|}{G\left(e^{-\alpha L} + e^{-\frac{\tau_F}{\tau}} \right) - A\left(1 + e^{-\alpha L}\right)}$$

(8)

To have an idea, we have plotted in Fig. 5 the FU as a function of the group velocity for a C Band section with the following typical parameters (see next section): L=1.5m, G=3, A=0.7, $\tau = 1\mu s$. The plot shows that, in a wide range of group velocity near $v_g/c \cong 0.02$, FU<10% and that there is a particular value of v_g/c for which FU=0. If v_g/c is lower than this value, the FU is dominated by the attenuation and the electric field at the entrance of the structure is higher than at the end.

Concerning the average dissipated power into the structure it is easy to verify that it is equal to:

$$p_{diss\_av} \cong P_{TW\_0}\left(1 - e^{-2\alpha L}\right)\left[\frac{G^2}{2\tau}\left(1 - e^{-2t_{SLED}/\tau}\right) - \frac{2AG}{\tau}\left(1 - e^{-t_{SLED}/\tau}\right) + A^2 t_{SLED} \right] f_{rep}$$

(9)

where t_{SLED} is the duration of the peak SLED pulse and f_{rep} is the repetition frequency of the pulses (in general the parameters are chosen in order to have $t_{SLED} = \tau_F$). The approximation in eq. (9) is that we have neglected the pre-pulse in the SLED.
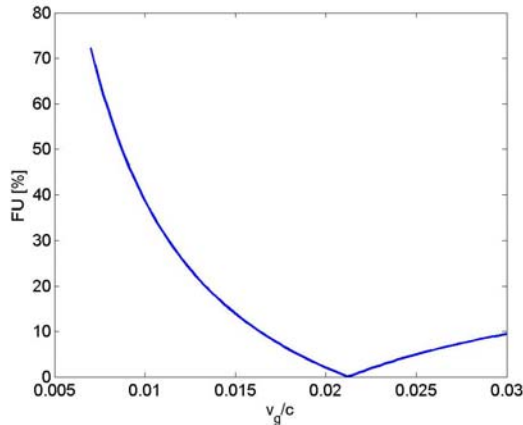
FIG. 5: FU as a function of the group velocity for a C Band section with the following typical parameters (see next section): L=1.5m, G=3, A=0.7, $\tau = 1\mu s$

2.3 Single cell optimization

The dimensions of the single cell have been optimized to simultaneously obtain:

a) the lowest peak surface electric field on the irises with the SLED input pulse;
b) an average accelerating field of (at least) 35 MV/m with the available power from the klystron;
c) the largest iris aperture compatible with the previous points in order to better pump the structure, to reduce the wakefields contribution and the filling time of the structure itself. This last point is related to the needed input pulse length to fill the structure and, therefore, with the breakdown rate probability [3] (at least from X Band) in the sense that a reduction of the pulse length strongly reduces the breakdown rate.

For our calculations we have considered the conservative parameters for the klystron and SLED system reported in TABLE II. For the SLED we referred to the parameters similar to the C Band SLED of SuperKEKB [18].

TABLE II: considered parameters for the klystron and SLED systems

Parameter	value
Q_0	130000
β	6
t_1	$2 \mu s$
G	3.18
A	0.71
τ	$1.034 \mu s$
P_{KLYout}	40 MW

The peak output power profile and the input power into the TW sections are given in Fig. 6. Fig. 7 shows the main structure figures of merit as a function of the iris aperture and thickness. In particular we have calculated: the average accelerating field (E_{acc_av}) after one filling time, the peak surface field ($E_{s\ peak}$) at the beginning of the RF pulse, the FU and the filling time of the structure itself. The peak surface field has been calculated in two different conditions. The first one is related to the case of the maximum input power that we considered available from the klystron (see Table II), the second one in the case we consider an average accelerating field of 35 MV/m.
Following the design criteria illustrated at the beginning of this paragraph and the results shown in Fig. 6 and Fig. 3, we decided to adopt an iris aperture of 7 mm with 2.5 mm thickness and an elliptical shape with $r_2/r_1=4/3$. The final dimensions are given in Fig. 8. In the final cell profile we have decided to round one sharp edge of the cell outer profile, in order to increase the quality factor as much as possible. This type of shape is compatible with the cell machining, as illustrated in the next section. The final structure parameters are given in Table III. They are referred to the final 1.4 m long structure and to the prototype we have built for high power test at KEK.
The sensitivity of the phase advance per cell as a function of the geometrical parameters is finally shown in Table IV. From these quantities it is possible to extrapolate the maximum tolerances of fabrication and correct with a proper cell tuning.
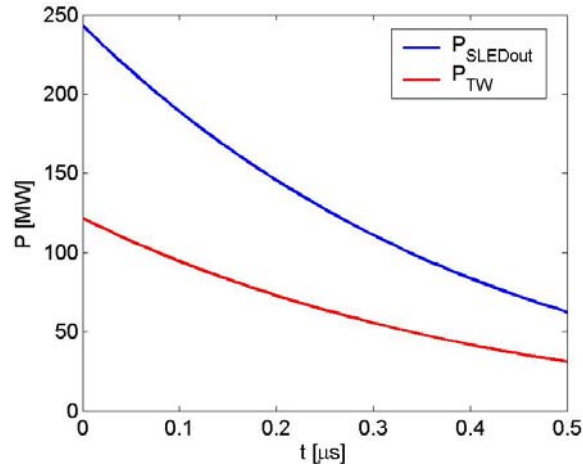
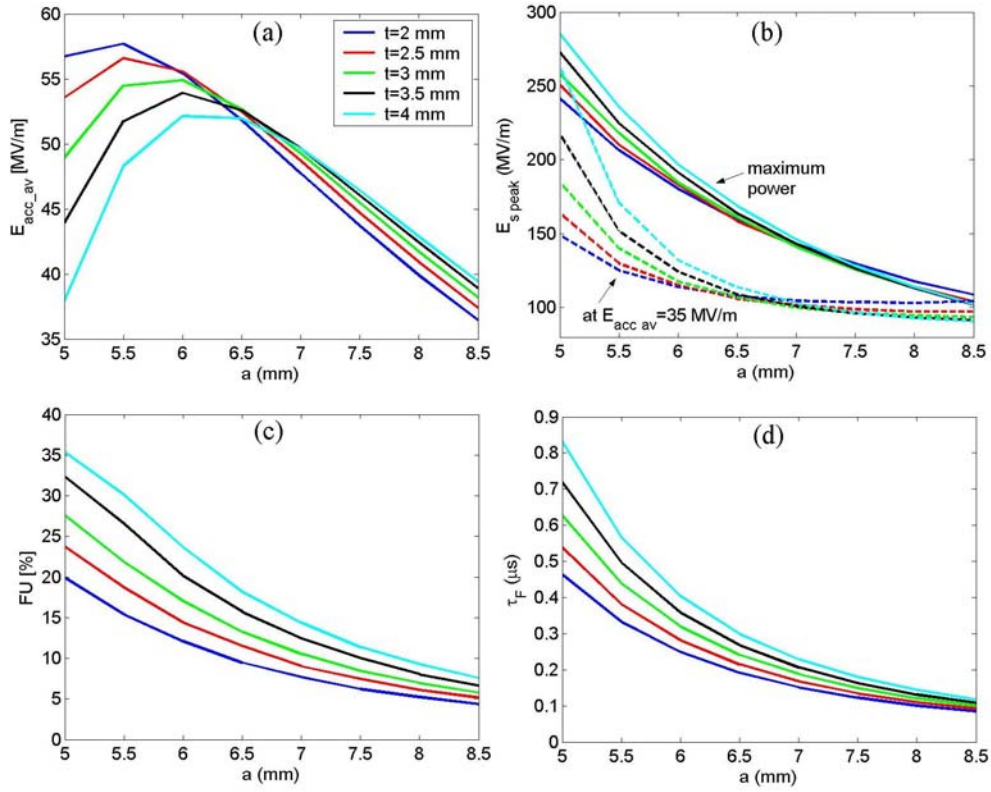FIG. 6: peak output power and input power into the TW sections.

FIG. 7: main structure figures of merit as a function of the iris aperture and thickness: (a) average accelerating field after one filling time; (b) peak surface field at the beginning of the RF pulse; (c) FU; (d) filling time of the structure.
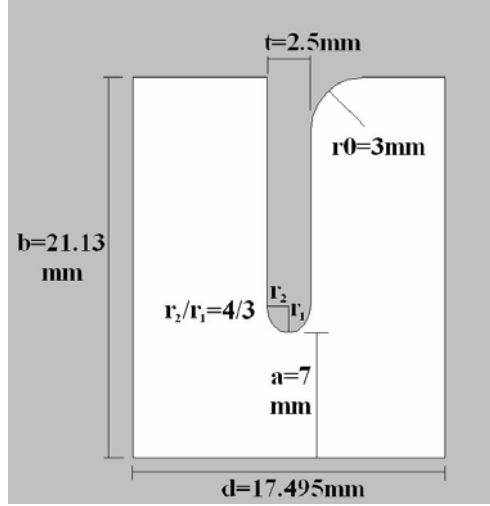
FIG. 8: Single cell final dimensions.

TABLE III: final structure parameters (HFSS results)

PARAMETER	prototype	Final structure
Frequency (f_{RF})	5.712 [GHz]	
Phase advance per cell	$2\pi/3$	
Number of accelerating cells (N)	22	71
Structure length included couplers (L)	0.54 [m]	1.4 [m]
Cell length (D)	17.495 [mm]	
Iris radius (a)	7 [mm]	
Iris thickness (t)	2.5 [mm]	
Outer radius (b)	21.13 [mm]	
group velocity (v_g/c):	0.0283	
Field attenuation (α)	0.206 [1/m]	
series impedance (Z)	34.1 [MΩ/m^2]	
shunt impedance (r)	82.9 [MΩ/m]	
Filling time (τ_F)	50 [ns]	150 [ns]
Power flow @ E_{acc}=35 MV/m	36 [MW]	
$E_{s\,peak}/E_{acc}$	2.17	
$H_{s\,peak}$ @ E_{acc}=35 MV/m	87.2 [kA/m]	
Pulsed heating @ E_{acc}=35 MV/m	<1 ^{o}C	
Average Accelerating field with SLED input pulse of Fig. 6 and after one filling time	60.2 [MV/m]	51.6 [MV/m]
Peak surface field with the pulse of Fig. 5 (at the beginning of the pulse) and with pulse scaled to have E_{acc}=35 MV/m	140 (96)[MV/m]	
Energy gain (max and @ 35 MV/m)	23.2 (13.5) [MeV]	64.1 (42) [MeV]
Output power	0.85·P_{in}	0.60·P_{in}
Average dissipated power @ 10 Hz with SLED pulse length equal to one filling time	7.6 [W]	59.6 [W]

TABLE IV: sensitivity of the phase advance per cell as a function of the geometrical parameters

Parameter	Sensitivity (deg/µm)
b	0.22
a	-0.062
t	-0.012
d	0.0087

5   COUPLER DESIGN

A wide and complete discussion on coupler design to minimize the surface magnetic field and, therefore, the coupler damage at high input power, is given in [8]. We adopted for our design the "waveguide coupler" that allows to simultaneously obtaining low pulsed heating [17] and a compact feeding system.

The sketch of the complete coupler with few TW cells is given in Fig. 9(a). The design has been divided in two parts, the coupler and the splitter. The first one has been designed by tuning the coupling iris and the outer radius of the first cell (shown in Fig. 8(b)) to match the waveguide mode TE_{11} with the accelerating mode TM_{01}-like. The design has been done using HFSS and following the procedure illustrated in [9]. As an example the amplitude and phase of the accelerating field and the accelerating field "seen" by a particle on crest are given in Fig. 10 for a 5 cell accelerating structure.

The splitter dimensions (shown in Fig. 8(c)) have been found by minimizing the reflection coefficient at the input port. Due to the symmetry of the system this simultaneously gave the optimization of the output splitted power.

The final obtained reflection coefficient was <-40 dB.

Concerning the peak magnetic field (and the related peak pulsed heating) on the coupler iris, it is lower than that in the single cell, as expected.
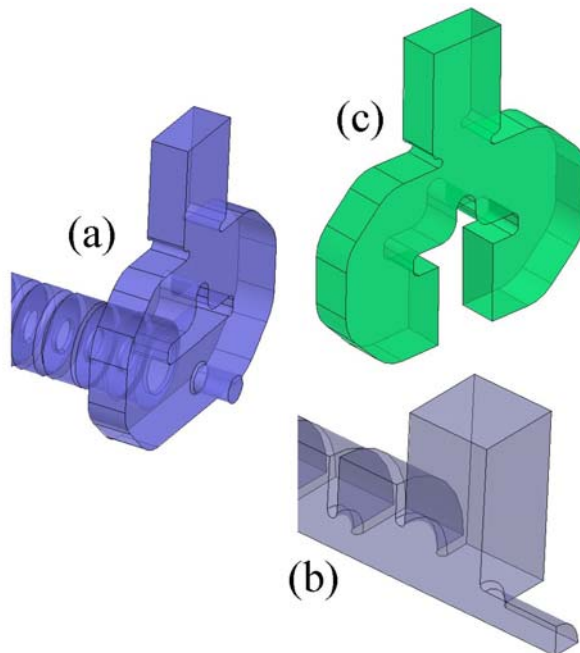
FIG. 9: (a) sketch of the complete coupler with few TW cells; (b) detail of the waveguide coupler; (c) detail of the splitter.
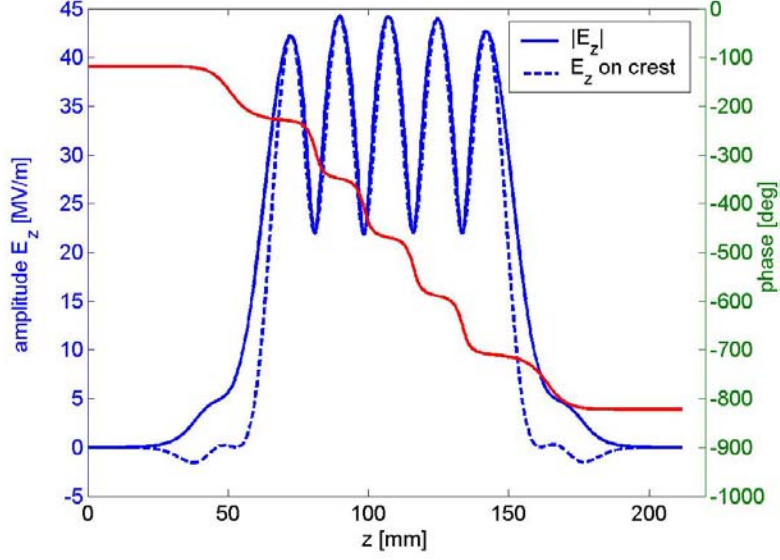
FIG. 10: Amplitude and phase of the accelerating field (5 cells structure) and accelerating field "seen" by a particle on crest.

An important point we have investigated in the design has been the evaluation of the field multi-polar components introduced by the waveguide coupler. The coupler, as a matter of fact, is a compact transition between a rectangular geometry (the waveguide) and a circular one and, therefore, it introduces multi-polar field components in the waveguide region. Due to the symmetric feed of the system these components have an even periodicity with respect to the azimuthal angle. More precisely the azimuthal magnetic field can be developed to first order as follows:

$$B_\varphi(r,\varphi,z) \cong A_o(z)r + \sum_{n=1}^{\infty} A_{2n}(z)\cos(2n\varphi)r^{2n-1}$$

(10)

where the A_{2n} components are complex functions and depend on the longitudinal coordinate z.

The quadrupolar component is the component associated to the term with n=1 and the gradient of the quadrupole component is exactly the term A_2.
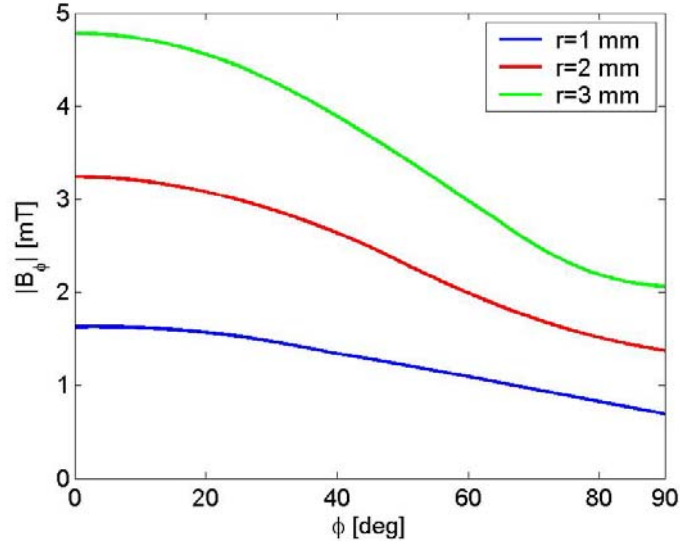
As an example the azimuthal magnetic field in the center of the waveguide coupler calculated on three circles of different radius is given in Fig. 11. In the calculation we have considered the case of an average accelerating field of 35 MV/m in the structure. From the plot it is easy to identify the quadrupolar profile (with 2φ dependence). Also other higher order components are present (octupole, decapole,…).

In principle it is possible to calculate all multi-polar components at different longitudinal coordinates by calculating the Fourier series components in different arcs. As a first order we have estimated the quadrupole gradient along the structure in the following way:

$$A_2(z) \cong \frac{B_{max}(r_0,z) - B_{min}(r_0,z)}{2r_0}$$

(11)

where B_{max} and B_{min} are the maximum and minimum of the magnetic field at a certain distance r_0 from the axis and at a given longitudinal coordinate z. The result is shown in Fig. 12 for r_0=3 mm where the absolute value of the quad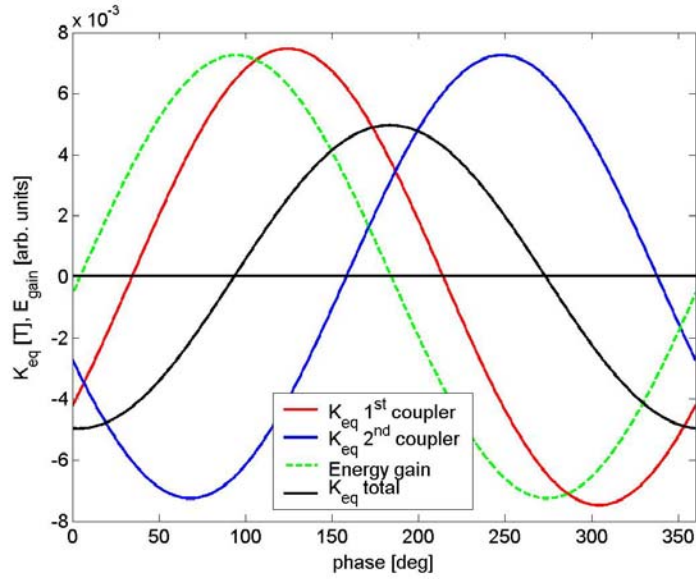rupole gradient has been plotted. The integrated quadrupole gradient in the first and second coupler (K_{eq}) as a function of the injection phase is shown in Fig. 13. In the same figure we have plotted the energy gain. It is straightforward to note that the two integrated quadrupole components have different phases with respect to the accelerating field.

All these results show that this quadrupole gradient is small if compared to usual magnetic quadrupoles but a further investigation of the effects on the beam dynamics have to be done. In particular Fig. 13 shows that this quadrupole component varies along the bunch.

The quadrupole component can be minimized by modifying the geometry of the coupler as shown in Fig. 14. The introduced bump changes this quadrupole amplitude and a minimum contribution (at least one order of magnitude smaller than the shown one) can be obtained.

FIG. 11: azimuthal magnetic field in the center of the waveguide coupler calculated on three circles of different radius.
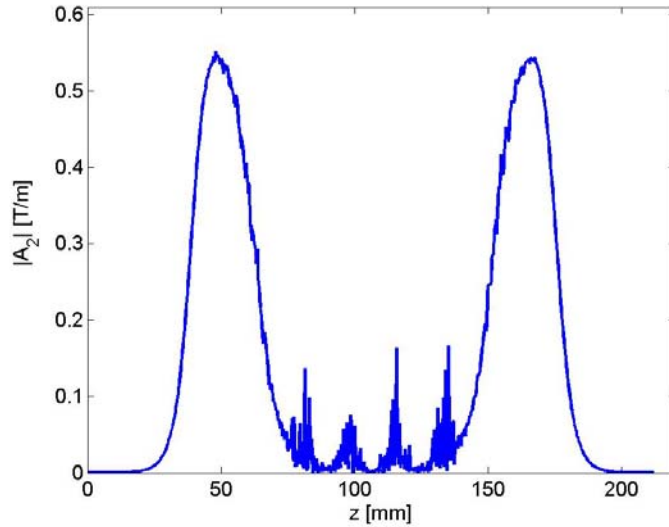
FIG. 12: absolute value of the quadrupole gradient calculated using equation (11) with r_0=3 mm

FIG. 13: integrated quadrupole gradient in the first and second coupler (K$_{eq}$) as a function of the injection phase
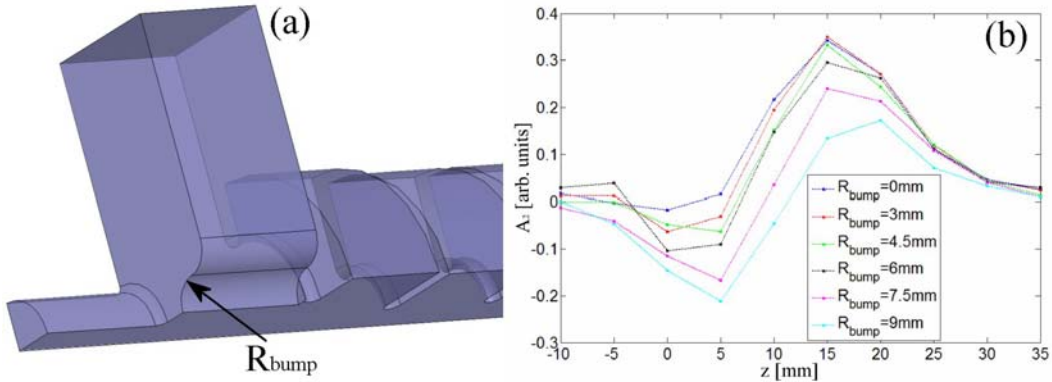
FIG. 14: bump on the waveguide coupler to minimize the quadrupole component of the field.

6   STRUCTURE REALIZATION

The final mechanical drawing of the prototype is given in Fig. 15. The input coupler includes the splitter while, for the output one, we decided to have two symmetric ports to be connected to two RF loads.

The mechanical drawing of the single cell is shown in Fig. 16 (a). Each cell has been machined as a "cup" and includes one iris. Fig. 16(b) shows the realized single cell. The cooling system has been integrated in each cell with 6 cooling pipes. Three tuners at 120° have been inserted. They allow deforming the outer wall of each cell in both directions. Each cell has been machined by a local company [11] with a high precision turning machine. The surface roughness was less that 50 nm while the precision on dimensions was ±2μm.

The input coupler has been realized in two halves with a computer controlled milling machine. The reached surface roughness was less than 200 nm with a precision in all

dimensions of ±10μm. The two halves have been assembled and brazed with the input flange. The picture of one of the two halves is shown in Fig. 17.

To minimize the number of brazing processes, the rectangular waveguide of the output coupler has been realized by an electron discharge machine. The coupling irises and the pipe have been turned by a computer controlled milling machine. The obtained surface roughness of the waveguide was less than 600 nm with precisions of ±20μm. The mechanical drawing of the output coupler and the realized one are given in Fig. 18.

The structure has been brazed in different steps at LNF. We have brazed the couplers with all flanges and the TW cells separately. Then we have brazed the full structure. The TW cells assembled and ready for brazing in the LNF oven are shown in Fig. 19 while the full structure is given in Fig. 20.
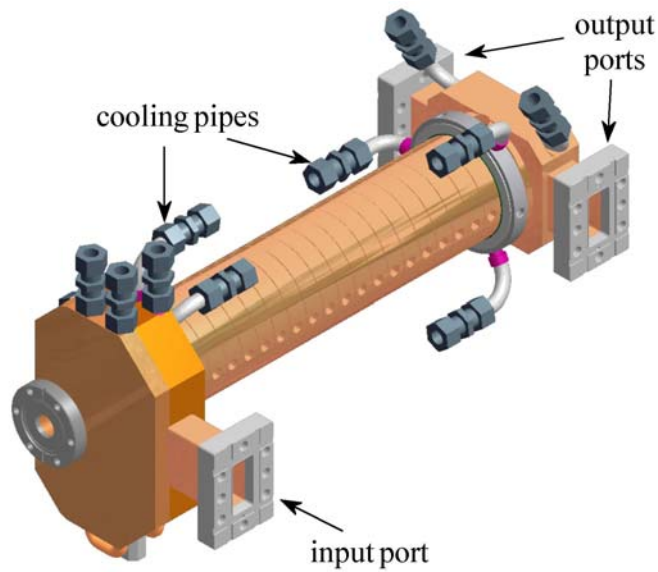
FIG. 15: mechanical drawing of the prototype.
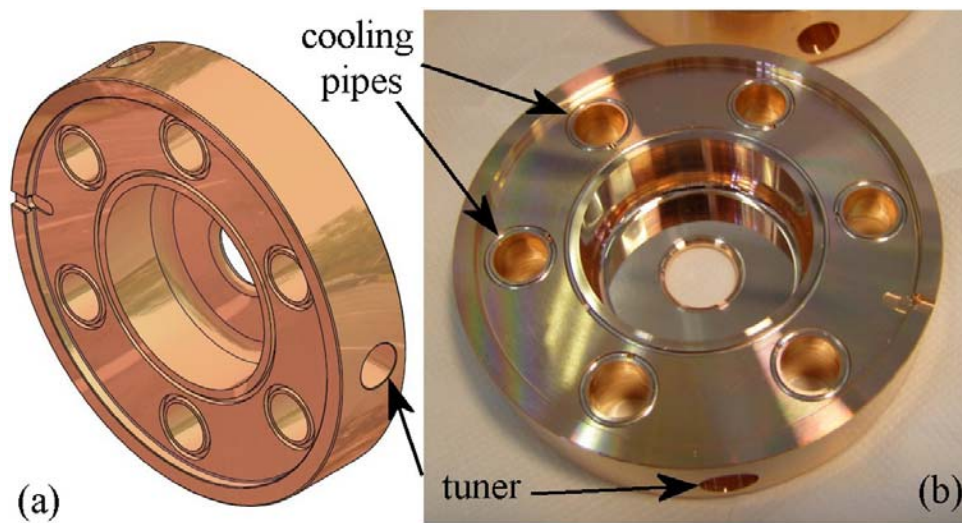
FIG. 16: (a) mechanical drawing of the single cell; (b) picture of the realized single cell.
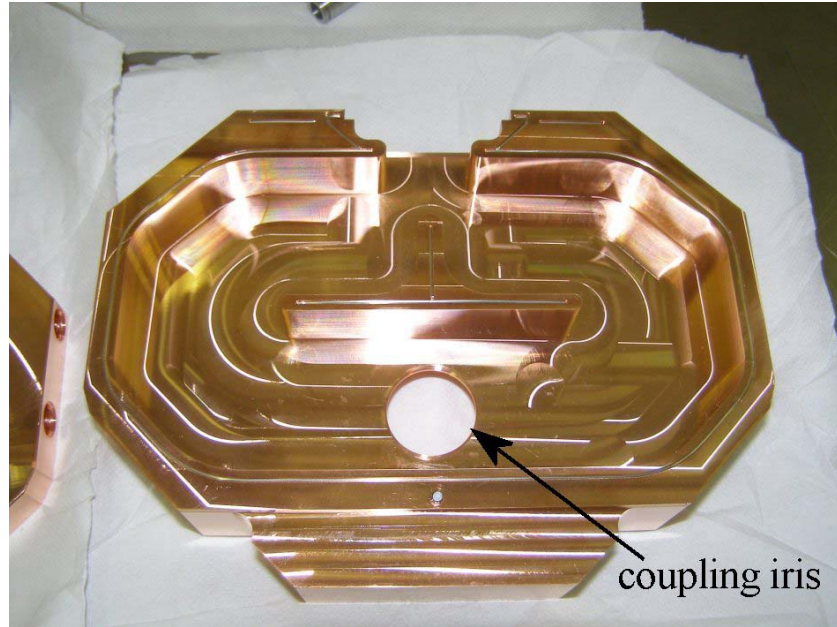
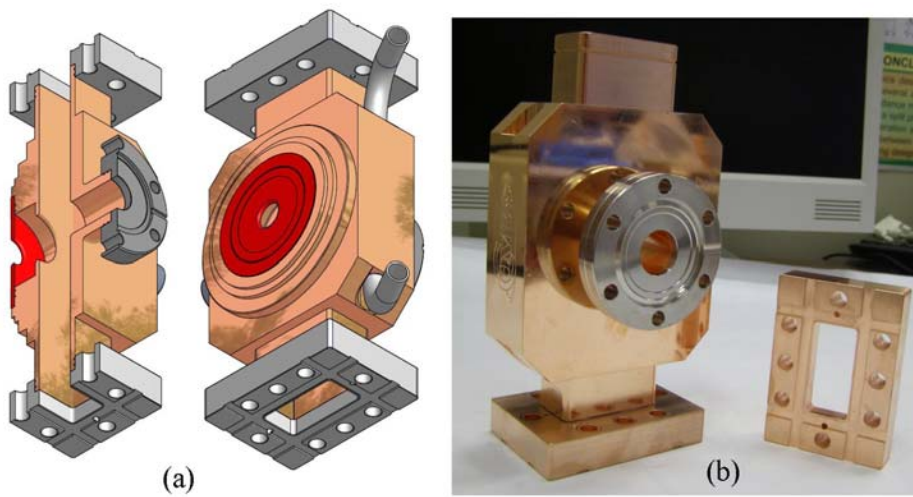**FIG. 17:** picture of one of the two halves of the input coupler.

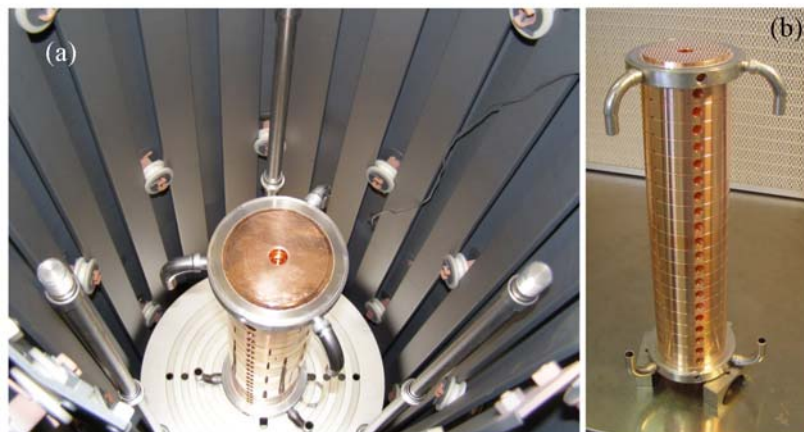**FIG. 18:** (a) mechanical drawing of the output coupler; (b) picture of the realized coupler.

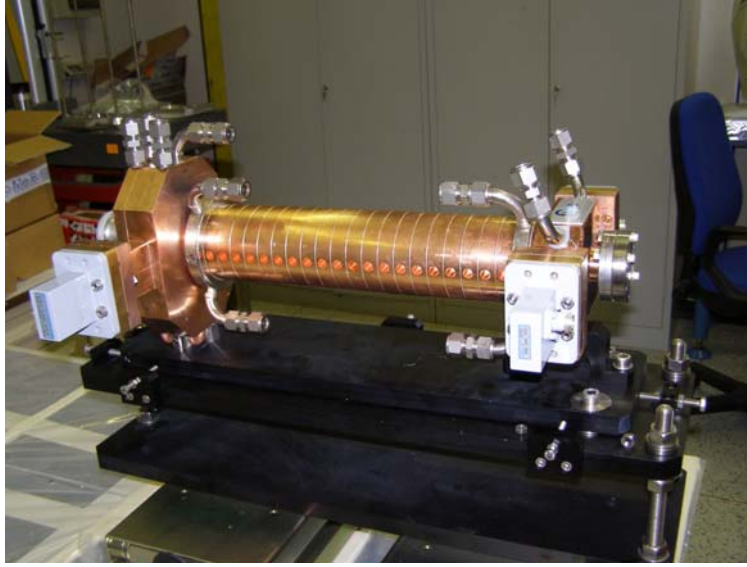**FIG. 19:** (a) TW cell in the LNF oven; (b) brazed TW cells.

FIG. 20: picture of the realized prototype.

7   RF MEASUREMENTS

RF measurements have been done at each brazing step and after the final brazing process. Fig. 21 shows the scattering parameters after the final brazing (port 1 is the input port, port 2 and 3 are the output ports). The expected S_{11} from HFSS simulations was less than 0.01 while the measured one was 0.078. The expected S_{21} and S_{31} were 0.647 while the measured ones were 0.641 and 0.648 respectively. We have measured also the longitudinal electric field (using the bead pull technique) and the result is given in Fig. 22. The field unflatness was about ±10%. The discrepancies between the simulated quantities and the measured ones were mainly due to the fact that the structure was not tuned. Moreover after the final brazing step we had some problems in the alignment between the TW cells and the couplers. In principle these problems could be overcome with the final tuning that will be done soon.
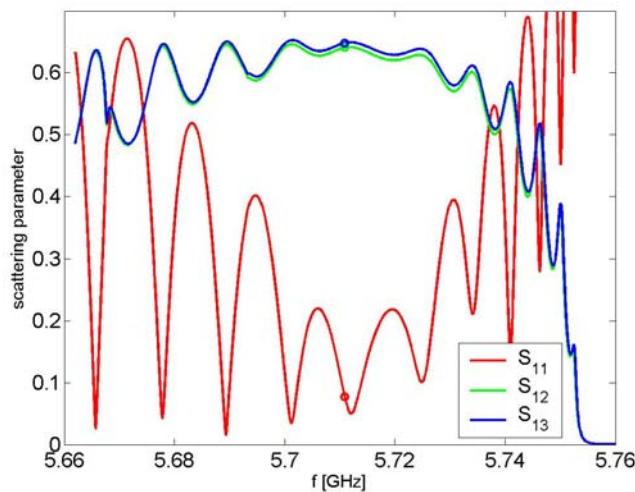

FIG. 20: scattering parameters after the final brazing (port 1 is the input port, port 2 and 3 are the output ports).
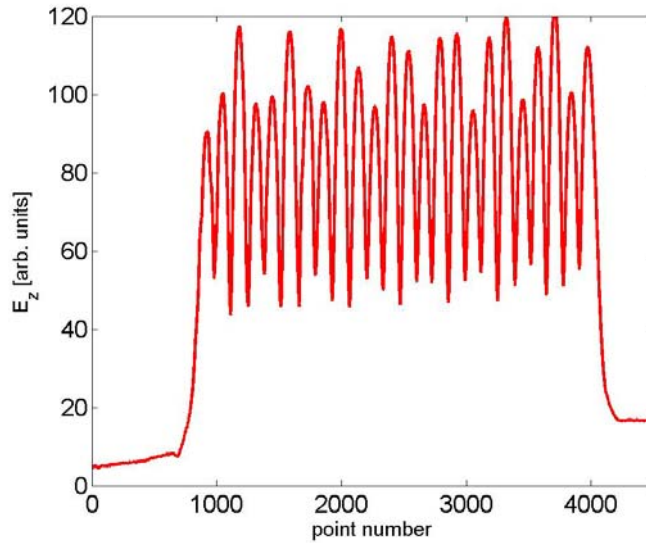
FIG. 21: measured electric field by bead pull technique on the final brazed structure.

8   CONCLUSION

In the paper we have presented the design of the structures operating at 5.712 GHz for the energy upgrade of the SPARC photo-injector. The structures have been conceived as traveling wave constant impedance sections. They have symmetric axial input couplers and have been optimized to work with a SLED RF input pulse.

A prototype with a reduced number of cells has been realized and characterized with low power RF measurements. It has been constructed for high power test at KEK.

ACKNOWLEDGEMENTS

REFERENCES

[1] 2. D. Farkas, et al., SLED: a method of doubling SLAC's Energy, SLAC-PUB-1453, 1974.

[2] Pierre M. Lapostolle and Albert L. Septier, Linear Accelerators, Eds. North-Holland, Amsterdam; Elsevier, New York, 1970

[3] see for example V.A. Dolgashev, High power tests of normal conducting single cell structures, Proceedings of PAC07, Albuquerque, New Mexico, USA, 2007.

[4] http://laacg.lanl.gov/laacg/services/

[5] G.A. Loew, et al., Computer Calculations for Travelling wave periodic structure properties, IEEE Transactions on Nuclear Science, Vol. NS-26, No. 3, June 1979.

[6] V. Spizzo, Progetto elettromagnetico di una struttura accelerante ad onda viaggiante in banda C, master degree thesis, Univ. Of Rome La Sapienza, 2009.

[7] www.ansoft.com

[8] Christopher Nantista, Sami Tantawi, and Valery Dolgashev, Low-field accelerator structure couplers and design techniques, PRST-AB, 7, 072001 (2004).

[9] D. Alesini, et al., Design of couplers for traveling wave RF structures using 3D electromagnetic codes in the frequency domain accoppiatori, Nuclear Instruments and Methods in Physics Research A 580 (2007) 1176–1183.

[10] J. LE DUFF : Optmization of TW accelerating structures for SLED type modes of operation (seminario a Frascati Marzo 1984 oppure LAL/RT/84-01 Feb. 1984).

[11] http://www.comeb.it/

[12] V. Fusco and M. Ferrario, Beam Dynamics study of a C-Band LINAC driven FEL with S-Band photo-injector, Proceedings of PAC09, Vancouver, BC, Canada.

[13] SwissFEL CDR, available at http://www.psi.ch/swissfel/.

[14] T. Shintake, Status Report on Japanese XFEL Construction Project at SPring-8, Proceedings of IPAC'10, Kyoto, Japan

[15] TIARA collaboration, http://www.eu-tiara.eu/information/index.php?id=13.

[16] D, Alesini, et al., Beam Energy upgrade of the Frascati FEL LINAC with a C-Band RF system, Proc. of IPAC 10, Kyoto, 2010.

[17] V.A. Dolgashev, High magnetic fields in couplers of X-Band Accelerating structures, Proceedings of the 2003 Particle Accelerator Conference, 2003.

[18] T. Sugimura, SKIP - A pulse Compressor for SuperKEKB, Proceedings of LINAC 2004, Lübeck, Germany, 2004.